Carbon 247 (2026) 121036

Contents lists available at ScienceDirect

Carbon

journal homepage: www.elsevier.com/locate/carbon

Influence of precursor structure on KOH-activated carbon: A study using tunable all-cellulose composites

Alexa Scheer [a], Glen J. Smales [b], Hoang Bao Tran Nguyen [d,e], Johannes Rattenberger [c], Claudia Mayrhofer [c], Johanna Fischer [d,e], Steffen Fischer [e], Daria Mikhailova [d,f], Stefan Spirk [a,*]

[a] Institute of Bioproducts and Paper Technology, Graz University of Technology, Inffeldgasse 23, 8010, Graz, Austria
[b] Institute of Inorganic Chemistry, Graz University of Technology, Stremayrgasse 9/IV, 8010, Graz, Austria
[c] Institute of Electron Microscopy and Nanoanalysis (FELMI), Graz University of Technology, Steyrergasse 17, 8010, Graz, Austria
[d] Leibniz Institute for Solid State and Materials Research (IFW), Dresden University of Technology, Helmholtzstraße 20, 01069, Dresden, Germany
[e] Institute of Plant and Wood Chemistry, Dresden University of Technology, Pienner Str. 19, Tharandt, 01737, Germany
[f] Karlsruhe Institute of Technology (KIT), Institute for Applied Materials (IAM), Hermann-von-Helmholtz-Platz 1, Eggenstein-Leopoldshafen, 76344, Germany

ARTICLE INFO

Keywords:
All-cellulose composites
Activated carbon
Precursor structure
KOH impregnation
One-step KOH activation
SAXS

ABSTRACT

Transforming cellulosic materials into activated carbon (AC) offers a promising route to valorize biowastes for applications requiring precise pore structures such as supercapacitors, gas separation, and storage. Yet, the impact of the precursor's structure on chemical activation with KOH remains insufficiently understood, limiting the reproducibility and optimization of AC properties. Systematic studies exploring how varying the structural properties of cellulosic precursors affect activation outcomes are lacking. Here, we demonstrate that incorporating regenerated cellulose microspheres (CMS) into a pulp fiber matrix significantly enhances KOH impregnation, yielding improved AC characteristics, including increased specific surface area (SSA) and optimized pore size distribution (PSD). WAXS and FTIR analyses confirmed that higher CMS content increases the amorphous regions within the semi-crystalline precursor. EDX mapping further showed superior KOH penetration into CMS-rich regions compared to the more limited interaction with pulp fibers. Consequently, TEM, SAXS, and N_2 adsorption analyses revealed that higher CMS content improves microporosity and increases SSA. Additionally, thermogravimetric analysis revealed that an uneven distribution of reactive, less crystalline CMS regions leads to localized over-activation, resulting in distinct changes in porosity. These findings demonstrate that the heterogeneous distribution of domains with differing crystallinity, typical of lignocellulosic materials, influences activation behavior and may partly explain the variability often observed in biomass-derived ACs. Our work establishes a clear mechanistic link from precursor structure to KOH accessibility and final pore architecture, demonstrating that precursor-structure engineering can effectively optimize AC properties and provides an often overlooked alternative to harsh activation conditions.

1. Introduction

Activated carbons (ACs) derived from biobased resources have attracted considerable attention for a variety of applications, such as gas separation and storage [1–5], catalysis [6,7], and energy storage [8–14]. These materials are particularly appealing because of their large specific surface area (SSA), hierarchical pore structures, and inherent chemical stability. For some applications like CO_2 capture and supercapacitor electrodes, well-defined pore structures are essential: ultramicropores (<0.7 nm) facilitate CO_2 absorption [4,15], while a combination of micropores (<2 nm) and mesopores (2–20 nm) provides high ion storage capacity and efficient ion transport in supercapacitors [8,9,12,13].

Recent studies show that one-step KOH activation generally produces higher SSAs and a more microporous structure compared to the traditional two-step route [16,17], but this comes at the expense of carbon yield (e.g., 2.5 % for one-step vs. 19.4 % for two-step using rice husk as precursor [18]). In the one-step approach, the biomass is directly impregnated with KOH and subjected to simultaneous carbonization

* Corresponding author.
E-mail address: stefan.spirk@tugraz.at (S. Spirk).

https://doi.org/10.1016/j.carbon.2025.121036
Received 11 August 2025; Received in revised form 19 October 2025; Accepted 3 November 2025
Available online 6 November 2025

and activation in a single thermal cycle. This combination reduces furnace time, lowers energy consumption, and simplifies operation for scale-up [16,19,20]. Achieving strong interaction and intimate contact between the precursor and KOH is crucial for producing AC with desirable properties. Unlike pre-carbonized char, cellulosic biomass is rich in oxygen-containing functional groups. These groups exhibit higher reactivity than carbon and interact readily with KOH, facilitating molecular-level impregnation [19,21,22]. Regenerated cellulose (cellulose II), with its lower crystallinity, leaves these functional groups much more accessible to KOH, whereas the tightly packed crystalline domains of native cellulose can impede solution penetration. Previous studies have shown that lower crystallinity in starting materials, whether carbon fibers [23] or lignocellulosic resources [24], leads to increased porosity in the resulting AC when produced using chemical activation agents.

Systematically adjusting activation parameters (e.g. temperature, impregnation ratio) in a Design of Experiment approach, allows precise control over yield, SSA, porosity, and elemental composition of AC produced from cellulose-based material [25]. However, the inherent batch-to-batch compositional differences and impurities in biomass feedstocks often lead to unpredictable AC properties, even under identical activation conditions [26]. The influence of precursor structure on AC characteristics, especially when chemical activators such as KOH are used, remains a point of debate [27–29].

Current research has not yet examined whether and how the relationship between the precursor's structural properties and AC porosity can be exploited to enhance AC properties. This paper addresses this research gap by exploring precursor-structure engineering as an alternative route to improve activation efficiency and tailor AC porosity. We employ well-defined all-cellulose composites in which the content of regenerated cellulose particles is systematically varied, allowing precise control over crystallinity and morphology. This model system enables us to isolate the effect of precursor structure on KOH interactions and the resulting AC properties, an aspect not previously examined in such a controlled way. Our approach offers a sustainable pathway to enhance activation outcomes without relying on harsher conditions such as higher temperatures, longer activation times, or increased KOH dosage. A further motivation for this study is the observation that activation results are frequently inconsistent even when identical conditions are applied. We propose that variations in the precursor structure play a central role in this variability by influencing how the activation agent interacts with the precursor, a relationship we aim to demonstrate here. Attention to these factors, and their adjustment where possible, could improve the reproducibility of AC synthesis from biomass.

The composites employed closely resemble laboratory-produced paper (e.g., hand sheets) and consist of two distinct cellulose components: cellulose microspheres (CMS) and pulp fibers. At the macroscale, these components differ in shape, representing spherical particles versus elongated fibers. At the microscale, they are distinguished by their cellulose allomorph type and crystallinity: regenerated cellulose II in CMS and native cellulose I in pulp fibers. Using CMS as the low-crystallinity component avoids the compositional heterogeneity that would arise if other biopolymers such as lignin were employed. This allows changes in the AC properties to be traced directly to structural variations rather than chemical differences. In addition, the spherical morphology of CMS enables them to function as fillers, a concept well established in papermaking. This facilitated their incorporation into sheets and ensured reproducible precursor formation. In a previous study, we confirmed the feasibility of producing CMS-containing paper sheets and showed that varying the CMS fraction significantly influences their structure, a finding that we build upon in the present work [30].

The precursor structure is characterized using wide-angle X-ray scattering (WAXS), scanning electron microscopy (SEM), inverse gas chromatography (IGC), and Fourier-transform infrared spectroscopy (FTIR). The interaction with KOH and thermal transformations during activation are investigated using penetration dynamics analysis (PDA) and thermogravimetric analysis (TGA). With constant activation parameters (temperature, duration, KOH:precursor mass ratio, and N_2 flow), this methodology enables a direct correlation between modifications in precursor architecture and changes in AC properties, which are subsequently characterized using SEM, transmission electron microscopy (TEM), small-angle X-ray scattering (SAXS), and nitrogen adsorption. Furthermore, it facilitates assessing whether increasing the amorphous fraction, achieved by incorporating higher CMS contents, improves activation outcomes.

2. Materials and methods

2.1. Materials

Commercial unbeaten bleached hardwood pulp from Lenzing (Lenzing, Austria) and CMS with a mean diameter of 1.5 µm (d50), produced following the method described by Thümmler et al. (2010) [31], were used to prepare the paper precursors. Activation was carried out using differently concentrated solutions of KOH (pellets, ≥85 %, Merck, Darmstadt, Germany), while 1 M HCl (Merck, Darmstadt, Germany) was used for the washing step after carbonization. All chemicals were used as received.

2.2. Preparation of ACs

The precursor papers (P0-P40) were produced using a Rapid-Köthen sheet former (FRANK-PTI, ISO 5269-2) following a method described in previous research of our group [30]. The CMS powder precursor (P100) was obtained by drying the CMS suspension used for papermaking at 80 °C overnight. All precursors were stored in a climatized room at 23 °C and 50 % relative humidity in accordance with ISO 187.

Precursors were impregnated using a pipette with a 30 w.% KOH solution prepared from a 50 w.% stock solution, while maintaining a paper-to-KOH weight ratio of 1:1. Directly after impregnation, four paper sheets of each type (P0–P40) were stacked in an Al_2O_3 crucible and placed in a three-zone tube furnace (TZF 15/610, Carbolite, Neuhausen, Germany). The CMS powder precursor (P100) was treated equivalently, with an equivalent mass placed in an Al_2O_3 crucible after impregnation.

The samples were then dried at 120 °C for 1 h under a nitrogen atmosphere (N_2 flow rate: 320 ml/min) using a heating rate of 5 °C/min. Afterwards, the temperature was increased to the activation temperature of 750 °C with the same heating rate and held constant for 1 h. Following the activation process, the samples were cooled under nitrogen flow and washed thoroughly with 1 M HCl and distilled water until the pH of the filtrate reached approximately 7. Finally, the AC samples (Table 1) were dried at 105 °C and stored in sealed containers to prevent moisture absorption (Fig. 1).

2.3. Characterization

2.3.1. Small angle x-ray scattering (SAXS)

SAXS data was collected using a SAXSpoint 2.0 instrument (Anton Paar, Austria). Scattering data was collected on an Eiger 1 M detector

Table 1
Description of the precursor samples and the derived ACs. The number following "P" or "AC" indicates the rounded CMS content in w.% in the paper.

Precursor	Rounded CMS content [w.%]	AC
P0	0	AC0
P10	10	AC10
P20	20	AC20
P40	40	AC40
P100[a]	100	AC100

[a] P100 = CMS powder, not a paper precursor.

(Dectris, Switzerland) using two sample-to-detector distances of 113 mm and 552 mm. X-rays were generated from a microfocused, monochromatized Cu Kα (λ = 0.154 nm) source and all AC samples were held in the beam between two pieces of Scotch Magic tape, while P samples were measured free standing. The resulting data was processed using the DAWN software package to an absolute scale, using standardized data correction procedures [32]. As the data was scaled to absolute intensity, a linear combination of the P0 and CMS data in the WAXS region could be used to estimate the volume and weight fractions of each component in the composite samples (P10, P20, P40) [33,34].

The scattering data for AC samples were analyzed using a combination of models in SASfit to describe the hierarchical porosity of the samples [35]. Model breakdowns for each sample and their corresponding fits can be found in the Supporting Information. The fits were subsequently utilized to calculate surface areas by analyzing the volume-weighted size distributions. The extracted size distributions were used to obtain cumulative volume-weighted distributions for each sample, and integrated contributions from all porous structures. Unlike N_2 adsorption, which depends on pore accessibility and adsorbate-surface interactions, SAXS measures the total internal and external surface area, independent of accessibility. Consequently, SAXS-derived surface areas are typically higher than BET values, especially for materials with extensive microporosity or restricted pore networks where diffusion limits N_2 adsorption. Further description of the methods used can be found in the Supporting Information, alongside discussion on potential sources of error.

2.3.2. Scanning electron microscopy (SEM)

SEM was performed on the paper and AC samples using a TESCAN VEGA3 microscope (TESCAN, Czech Republic) equipped with a secondary electron detector. The microscope was operated at an acceleration voltage of 3 kV, with a tungsten cathode serving as the electron source. Before imaging, the paper samples were coated with a thin layer of gold using a Cressington 108 Auto Sputter Coater for 60 s to enhance conductivity.

2.3.3. Penetration dynamics analysis

KOH solution uptake of the paper samples (P0-P40) was characterized with a Penetration Dynamics Analyzer 2.0 (PDA, emtec Electronic GmbH, Leipzig, Germany). Specimens measuring 5 × 7 cm were secured on the holder using double-sided adhesive tape and then quickly submerged in the solution. A 2 MHz ultrasonic beam traversed a 35 mm-diameter sensing zone, and its transmission was recorded over time. As capillary absorption progresses, the transmitted signal gradually weakens. The rate of this signal decline therefore serves as an indicator of the liquid penetration speed.

2.3.4. Inverse gas chromatography (IGC)

For the IGC analysis, about 250 mg of the CMS and 170–190 mg of paper stripes (P0-P40) were packed into an empty, salinized glass column (SEA standard column with 4 mm inner diameter and 30 cm length) and plugged by salinized glass wool. Before the measurement, all samples were conditioned at 30 °C for 1 h. Decane, nonane, octane, and heptane were injected as dispersive probes across fractional surface coverages (Q = 0.005–0.2 n/nm) to determine the dispersive surface free energy (SFE) profile. The specific SFE was determined using dichloromethane and ethyl acetate over the same range of fractional surface coverages as the dispersive probes. All experiments were conducted at 30 °C with an N_2 carrier gas flow rate of 10 ml/min, using methane for dead volume corrections. All parameters of the used adsorbents were obtained directly from the SEA Analysis software provided by Surface Measurement Systems Ltd, UK.

2.3.5. Attenuated total reflection Fourier-transform infrared spectroscopy (FTIR)

FTIR spectroscopy was conducted on the precursor materials using an Agilent Cary 630 FTIR Spectrometer (Santa Clara, CA, USA) equipped with an ATR diamond module. Spectral scans were performed over the range of 4000 to 650 cm^{-1}, with each measurement consisting of 64 averaged scans. The resulting data was then analyzed using Origin Pro 2020 software.

2.3.6. Thermogravimetric analysis (TGA)

Thermogravimetric analysis (TGA) was performed on a Netzsch 449-F1 Jupiter instrument (Netzsch, Selb, Germany) to examine the thermal decomposition of the KOH-impregnated precursors. Approximately 20 mg of each sample was weighed into a ceramic crucible and heated from 30 °C to 750 °C at a rate of 5 °C/min under a continuous nitrogen atmosphere. Upon reaching 750 °C, the sample was held at this temperature for 1 h to simulate the activation in the tube furnace.

2.3.7. Energy-dispersive X-ray spectroscopy (EDX)

Cross-sections of dried paper samples impregnated with KOH were prepared by embedding them in 'Epofix' resin (Struers GmbH, Willich, Germany). After the resin had completely cured, the cross-sections were prepared using the ultramicrotome Leica UC6 NT (Leica Microsystems, Vienna, Austria), which was equipped with a histo diamond knife (Diatome Ltd., Biel, Switzerland). Microstructural characterization and elemental analysis were conducted using a ZEISS Sigma VP 300 electron microscope (Carl Zeiss, Oberkochen, Germany), which features a Schottky-type field emission source. Imaging and analysis of the cross sections were performed in low vacuum mode (40 Pa N_2 as imaging gas) at an accelerating voltage of 10 kV. Elemental compositions were determined via energy-dispersive X-ray spectroscopy (EDX) using an integrated silicon drift detector (SDD) from Oxford Instruments (Oxford, UK).

2.3.8. Nitrogen adsorption experiments

Nitrogen (N_2) adsorption experiments were conducted using a Quadrasorb SI (Quantachrome Instruments) at a temperature of −196 °C (77 K). Prior to the measurements, approximately 25 mg of each sample was degassed under dynamic vacuum conditions at 150 °C for 24 h using a FloVac degasser. The SSA was determined within the relative pressure range of p/p_0 = 0.05–0.3, applying the multi-point Brunauer-Emmett-Teller (BET) method [36]. The SSA of micropores was calculated through the t-plot method [37], the PSD was analyzed using the Quenched Solid Density Functional Theory (QSDFT) model for slit-shaped and cylindrical pores [38,39].

2.3.9. Transmission electron microscopy (TEM)

Transmission electron microscopy (TEM) measurements of the fabricated ACs were carried out by briefly dipping a 300-mesh copper grid, coated with a lacy carbon film, into a well-dispersed AC–acetone mixture (1:1000, w/w). After the solvent has been evaporated, the grid was mounted on the TEM holder. A JEM-2800 (JEOL, Akishima, Tokyo, Japan) operated at 200 keV was used for imaging, and micrographs were recorded on an ORIUS SC200 CCD camera (GATAN, Pleasanton, CA).

3. Results and discussion

3.1. Precursor manufacturing and properties

To produce the precursor papers (P0–P40), a defined volume of fiber suspension was combined with a precise mass of CMS suspension, followed by the addition of a retention agent solution. After thorough mixing, the slurry was formed into sheets using the Rapid-Köthen sheet former, dewatered, and dried for 10 min. For high CMS contents (≥10 w.%), a surplus of CMS suspension was added based on the CMS retention. This method enabled the production of stable paper sheets with CMS weight fractions significantly exceeding those typically achievable with conventional inorganic fillers [30].

The CMS content in w.% of the precursor papers was determined

based on the dry mass of the formed sheets using the known dry fiber masses with equation (1), as well as through linear combination of the WAXS data from pure CMS (P100) and pure fiber (P0) samples (see SI).

$$CMS\ content = \frac{sheet\ mass - fiber\ mass}{sheet\ mass} \quad (1)$$

Fig. 2, a shows good agreement between the calculated CMS contents and those determined from linear combination of WAXS measurements: P10 = 7.1 w.% (calculated) vs. 8.8 w.% (WAXS); P20 = 21.1 w.% vs. 18.4 w.%; and P40 = 36.2 w.% vs. 39.7 w.%. Minor discrepancies between the calculated and WAXS-derived values likely arise from uncertainties in the fiber mass estimation used in equation (1). During papermaking, the desired fiber mass is obtained by taking a calculated volume from a well-mixed fiber suspension of known pulp concentration. However, slight inaccuracies in the sampled volume or insufficient mixing can cause deviations from the desired fiber mass, leading to discrepancies in the calculated CMS content. In contrast, the CMS content determined by WAXS through linear combination of the crystalline and amorphous phases likely provides a more accurate reflection of the actual CMS content in the precursor papers. To improve readability, CMS contents in the precursor papers are referred to as values rounded to the nearest ten percent in the discussion below.

The wide-angle X-ray scattering (WAXS) analysis reveals how the semicrystalline structure of our paper precursors evolves as pulp fibers (cellulose I) are progressively replaced by CMS (cellulose II). The scattering profile of the unmodified sample (P0) features a prominent reflection at q ≈ 16 nm^{-1}, corresponding to the (200) plane of cellulose I. A distinct doublet between q ≈ 10 and 12 nm^{-1}, attributed to the (1–10) and (110) planes further indicates parallel-chain packing typical of native cellulose. With increasing CMS content (samples P10–P40), the cellulose I (200) peak shifts toward lower q values (≈15 nm^{-1}), indicating structural reorientation towards the (020) plane and the disruption of native chain alignment. The reflection at q ≈ 14 nm^{-1}, associated with the (110) plane intensifies, while the characteristic doublet between 10 and 12 nm^{-1} becomes less pronounced. These changes point to altered interplane spacings. In samples with higher CMS concentrations (P20–P100), a new reflection emerges at a lower angle, q ≈ 8.5 nm^{-1}, attributable to the (1–10) plane of cellulose II. The growing intensity of this peak confirms the conversion to antiparallel chain packing and highlights the expanded intersheet spacing characteristic of cellulose II [40–42]. Overall, the WAXS data indicate a gradual decrease in crystallinity and an increasing presence of cellulose II domains as pulp fibers are replaced by CMS. This trend is quantified by the crystallinity index, calculated from the characteristic WAXS peak at 15.66 nm^{-1} using the Segal method, which decreases from 79.8 to 76.0 with increasing CMS content (P0 to P100). The crystallinity index serves as a measure for comparing the composites but should not be interpreted as an absolute value. Further details on the Segal calculation are provided in the Supporting Information.

The integration of CMS into the pulp fiber matrix has a profound impact on the microstructure of the composite precursor. At low CMS content (10 w.%, P10, Fig. 3c and d), the microspheres tend to accumulate around the pulp fibers. This is facilitated by the protruding fibrils on the fiber surfaces, which serve as anchoring points, suggesting a high degree of adhesion between the CMS and the fiber network. As the CMS content increases to 20 w.% (P20, Fig. 3e and f), the CMS begin to form bridges between adjacent fibers, increasing the connectivity within the network. At the highest CMS loading (40 w.%, P40, Fig. 3g and h), the CMS aggregate into large, densely packed clusters, creating compact domains within the fiber matrix. Some of these CMS-rich regions effectively close inter-fiber voids, significantly increasing the overall density of the composite. The once-open fiber network becomes compact, which influences not only density but also KOH transport properties. In contrast, when pulp fibers are absent (P100, Fig. 3i and j), the CMS are unable to form a connected network. Instead, the microspheres aggregate into large, irregularly shaped clusters that remain discrete, failing to establish an interconnected morphology.

The PDA measurement using KOH solution demonstrates distinct wetting behaviors among paper samples with varying CMS content. Samples containing 0–20 w.% CMS (P0–P20) exhibited rapid and near-instantaneous penetration, as reflected by a signal drop occurring within the first 0.5 s (Fig. 4, a). This behavior indicates excellent wettability and minimal resistance from surface or capillary barriers, suggesting that CMS incorporation up to 20 w.% does not significantly alter the accessible pore structure or hydrophilic properties of the paper. In contrast, the P40 sample showed considerably slower penetration kinetics, characterized by delayed signal attenuation and substantially increased variability among measurements (Fig. 4, b). These slower penetration rates further demonstrate that high CMS concentrations notably affect KOH transportation by reduced porosity of the paper. The SEM images of P40 (Fig. 3g and h) clearly show substantial pore blockage. However, image analysis based on SEM micrographs revealed only minor differences in surface porosity between P20 and P40, 22 % vs. 19 % at 500 × magnification and 26 % vs. 25 % at 3000 × magnification (see Supporting Information for details). This modest variation does not reflect the pronounced difference observed in KOH penetration rates, which is not unexpected given that SEM images provide information limited to the surface and represent only a very small area of the sample. In contrast, our previous study demonstrated through air permeability measurements that high CMS loadings significantly reduce the bulk porosity of the paper, which more plausibly accounts for the pronounced reduction in KOH penetration speed [30].

As shown in Fig. 5 a, incorporating CMS into the pulp-fiber network increases the SSA, reaching its peak at 40 w.% CMS. The fibers act as a framework that separates microspheres and anchors them to fibrils on the fiber surfaces. This hierarchical architecture, fiber surface → fibril → microsphere, creates a large amount of externally accessible surface, resulting in a rising SSA with increasing CMS content. Once the fiber scaffold is removed (P100), however, the CMS lose these anchoring points and fuse into agglomerates. A substantial fraction of their surface is then locked in sphere-sphere contacts, causing the measured SSA to decrease despite the higher CMS mass fraction. Thus, it is not the quantity of CMS but its dispersion and accessibility within the composite that governs the SSA.

The SFE of the paper precursors was measured by adsorption of probe gases at low fractional coverage (0.005 n/nm^2) and was found to decline as CMS loading increased from P0 to P40 (Fig. 5, b). While a lower SFE can impede KOH uptake, the small SFE difference between P20 and P40 cannot explain the large gap in their absorption rates as reflected in the PDA measurements (Fig. 4). Instead, the reduced porosity of P40, caused by CMS filling and closing of interfiber voids, appears to be the primary factor limiting the rate of alkali penetration. The decline in SFE with increasing CMS loading can be attributed to two main effects: first, the CMS particles occupy hydroxyl groups on the fiber surfaces, and second, the CMS themselves may intrinsically possess a lower SFE compared to the cellulose fibers. This could be a result from their multi-step synthesis. They are prepared by dissolving cellulose acetate and then emulsifying this solution in an aqueous phase containing salt, protective colloids, and surfactants. Vigorous mixing with a high-speed disperser generates fine droplets of cellulose acetate, which subsequently precipitate once the solvent is removed. The resulting cellulose acetate beads are then deacetylated in sodium hydroxide solution to yield regenerated cellulose microspheres, followed by multiple washing steps to remove residual chemicals [31]. Factors arising from this process, such as residual surfactants or incomplete deacetylation can collectively diminish their hydrophilicity.

FTIR analysis (Fig. 6) reveals pronounced differences in hydrogen bonding between papers containing CMS and those without (see Fig. 1). In the O–H stretching region (Fig. 6 a), P40 exhibits characteristic band features of pure CMS, with O–H bands shifting to higher wavenumbers (blue shift). This shift suggests the formation of new, shorter, and weaker hydrogen bonds between the fibers and CMS [43]. Furthermore,

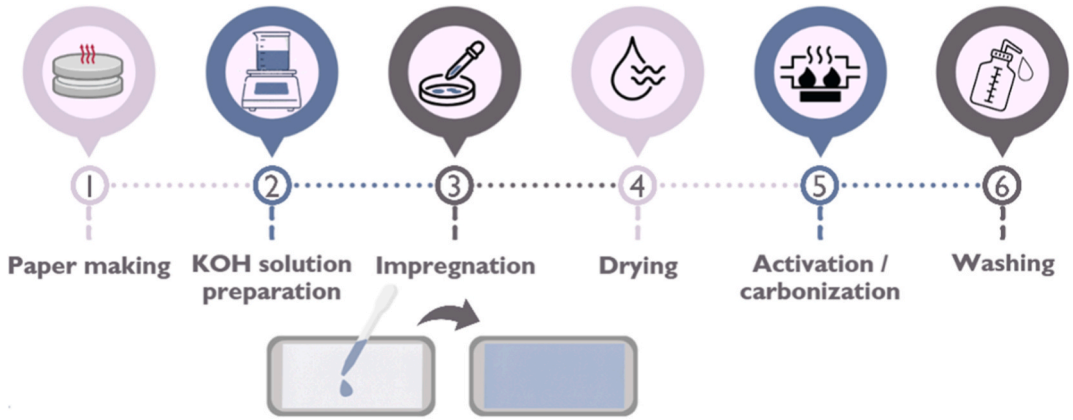

Fig. 1. Scheme of the used AC production method.

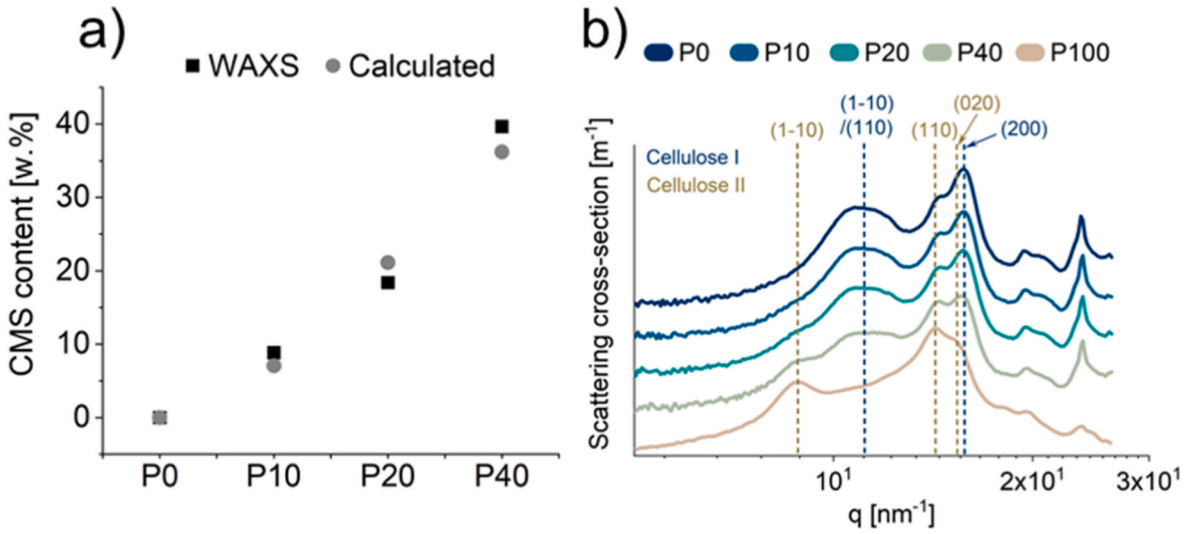

Fig. 2. (a) Comparison of the CMS content in the fabricated precursor papers, as determined by calculation (equation (1)) and by linear combination analysis of WAXS data. (b) WAXS patterns of the precursor materials.

the absence of a pronounced band near 1740 cm^{-1} [44] (Fig. 6, c) suggests that residual acetyl groups, if present, exist only in trace amounts and/or are masked by overlapping bands. In the fingerprint region (Fig. 6, b), characteristic cellulose bands appear at 1426 cm^{-1} (–CH_2 symmetric vibration), 1364 cm^{-1} (C–H bending), 1333 and 1314 cm^{-1} (CH_2 wagging and OH deformation), 1200 cm^{-1} (C–O–C symmetric stretching and OH plane deformation), 1159 cm^{-1} (C–O–C pyranose ring vibration), and in the region of 1103–1000 cm^{-1}, corresponding to C–OH, C–C, and C–H ring and side-group vibrations [45–48]. In CMS-rich samples (P40 and CMS), the 896 cm^{-1} band (C–O–C stretching in the β-glycosidic linkage) is more intense compared to P0, indicating increased amorphous character [47]. The intensity of 1103 and 1426 cm^{-1} bands are decreased in these samples, further indicating a growth of amorphous regions. Variations in the 1314–1364 cm^{-1} range, along with a decrease in the 1051 cm^{-1} band intensity, point to changes in intramolecular and intermolecular hydrogen bonding. The shifts from 1027 to 1019 cm^{-1} and from 986 to 995 cm^{-1} may suggest torsional alterations in the glycosidic linkage [48]. The structural reorganizations observed by FTIR with increasing CMS content align with the decrease in crystallinity determined by WAXS (Fig. 2).

3.2. *Precursor properties after KOH impregnation*

Fig. 7 presents SEM images (backscattered electron, BSE) and corresponding EDX mapping of cross-sections from KOH-impregnated samples P0 to P100. Low magnification BSE-SEM images (Fig. 7, column 1) were obtained at slightly different magnifications to maintain comparable cross-sectional views, as paper thickness decreases with increasing CMS content. These images clearly show that sample P40 exhibits the most heterogeneous CMS distribution, marked by a thick layer of potassium-rich microspheres on one side (highlighted in Fig. 7, j). The tendency of CMS to accumulate on one side of the precursor papers at higher concentrations was also observed in our previous work [30]. Conversely, samples P10 and P20 display more uniform macroscopic potassium distributions, correlating with their even CMS distribution. The BSE images at higher magnification (Fig. 7, column 3) indicate that after 1 h of drying under nitrogen, CMS lose their spherical shape and fuse together due to the reaction with KOH. This morphological change signifies their conversion to alkali cellulose.

The EDX mapping images (Fig. 7, column 2) reveal clear differences in the local distribution of potassium. Regions rich in CMS exhibit significantly higher potassium concentrations, while the interiors of pulp fibers show much weaker potassium signals. These findings support the hypothesis that CMS have a greater capacity for KOH uptake than fibers. Sample P0 displays a pronounced potassium concentration

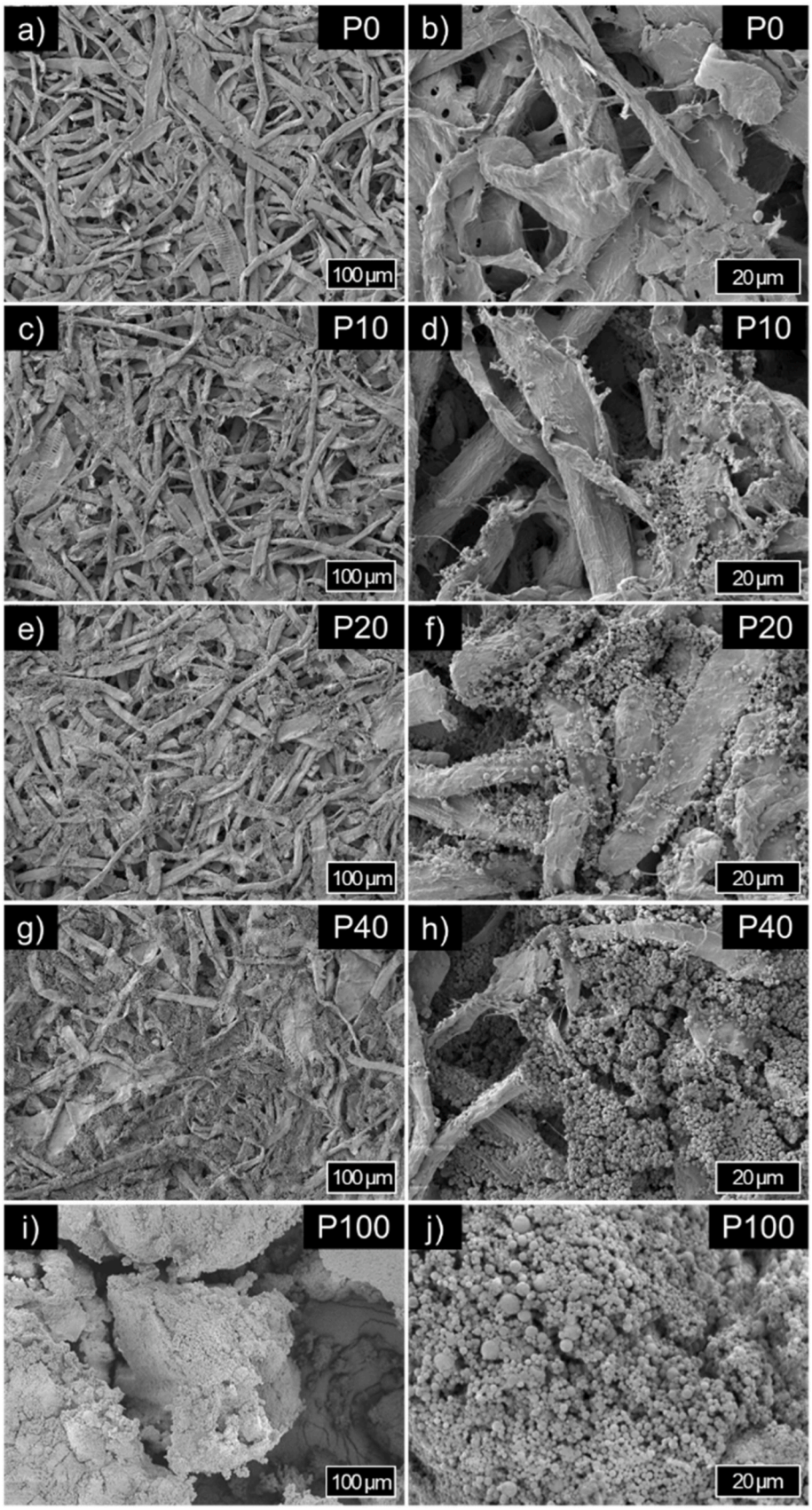

Fig. 3. Comparison of microstructures observed by SEM for papers containing 0 w.% CMS (a, b), 10 w.% CMS (c, d), 20 w.% CMS (e, f), 40 w.% CMS (g, h) and 100 w.% CMS (i, j), shown at 500 × magnification (a, c, e, g, i) and at 3000 × magnification (b, d, f, h, j).

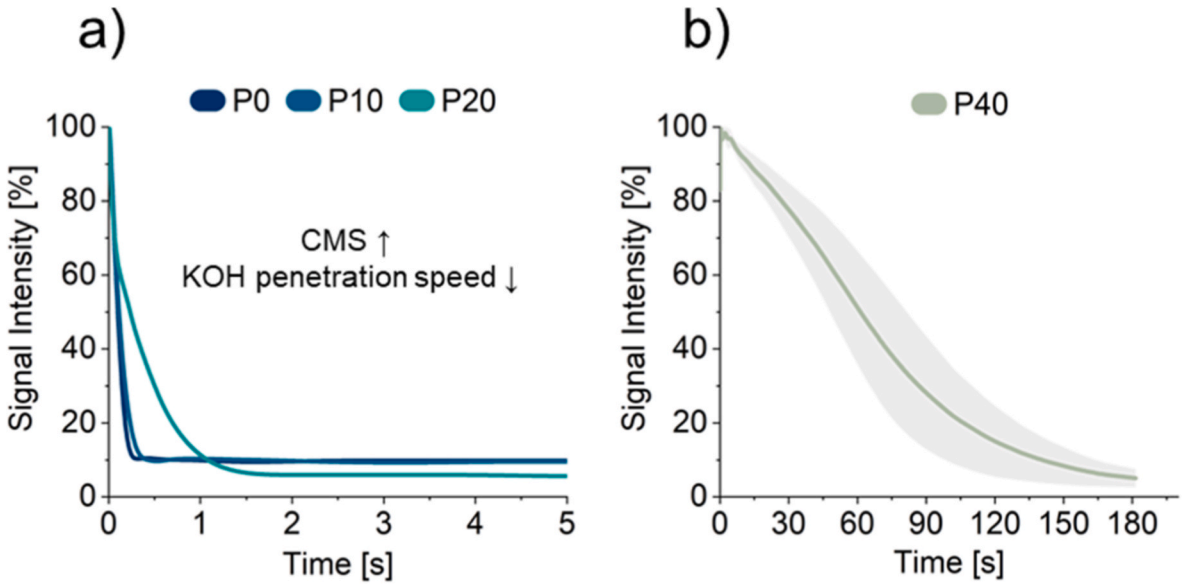

Fig. 4. Determined KOH solution penetration dynamics of (a) P0-P20 and (b) P40.

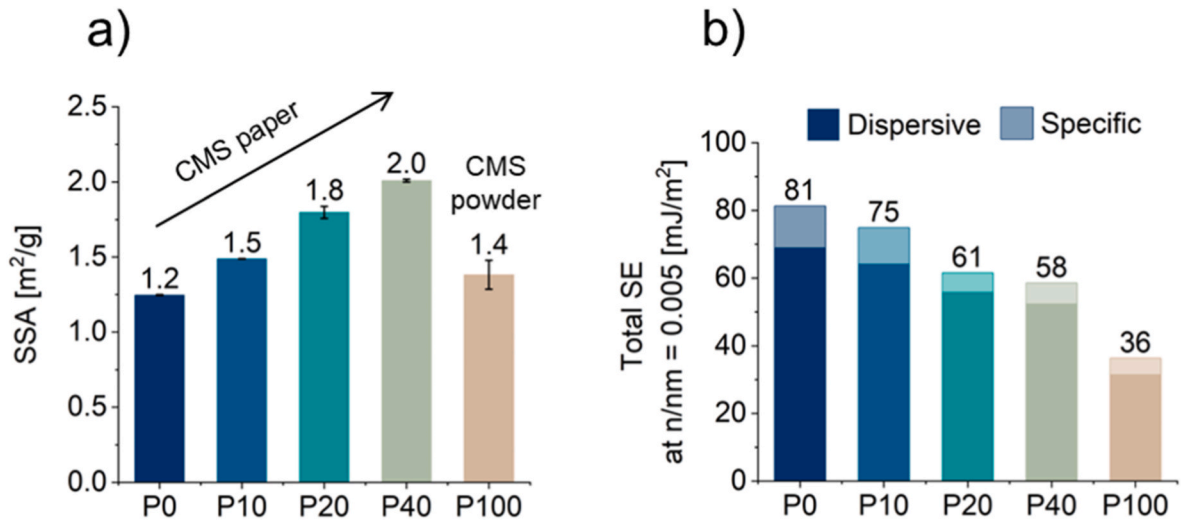

Fig. 5. SSA (a) and SFE (b) of precursors determined by IGC measurements.

contrast between fiber interiors and exteriors. In comparison, this contrast diminishes in P10, indicating enhanced potassium penetration into fiber interiors, possibly due to altered capillary forces. Definitive conclusions, however, require further investigation. Both P20 and P100 exhibit relatively uniform potassium distribution within microsphere-rich regions. In P100, dark areas correspond to voids between fused particles, as indicated by the BSE image (Fig. 7, o). Sample P40 shows localized regions of intense potassium concentration within CMS domains (Fig. 7, k). This heterogeneity in potassium distribution in P40 correlates with its reduced KOH uptake kinetics, as measured by PDA (Fig. 4). The higher bulk density of P40 restricts fluid transport, while simultaneous water evaporation further limits KOH mobility, leading to solidification and hindering uniform potassium distribution. Consequently, this uneven potassium distribution, together with the potassium-rich CMS surface layer, may lead to non-uniform activation and, as a result, influence the pore development in the final AC.

Thermogravimetric analysis (TGA) of the KOH-impregnated paper precursors reveals a sequence of mass-loss events that reflect moisture evaporation, chemical transformations, and carbonization. Between 30 °C and 170 °C, water evaporation dominates the mass loss, accompanied by the onset of KOH-mediated mercerization: KOH swells the precursor components, lowers crystallinity, and forms alkali cellulose by anchoring K^+ ions within the polymer network. Variations in initial moisture content among samples lead to differing mass losses, causing vertical offsets in their TGA curves [49]. From 170 °C to 230 °C, all samples lose about 7–8 % mass by partial glycosidic bond breakage and dehydration, releasing low-molecular-weight species and gases (H_2O, CO_2, CO) [49,50]. DTG curves show that higher CMS content slows the mass-loss rate, probably because of impeded volatile diffusion through CMS particles and narrowed inter-fiber pores. As the temperature rises above 360 °C KOH starts to melt, enhancing its mobility and enabling deeper diffusion into the components [51]. PDA demonstrated complete wetting within seconds to minutes; however, the hydrated K^+ ion, surrounded by a large solvation shell, initially accesses only pores wide enough to accommodate this shell. Upon melting all water is gone, reducing the effective radius to that of the bare K^+ ion. Together with the enhanced mobility of the molten salt, this size reduction allows potassium to diffuse into microstructural regions previously inaccessible. Sample P40, which has the most heterogeneous potassium distribution (Fig. 7, j), exhibits a pronounced mass loss between 320 °C and

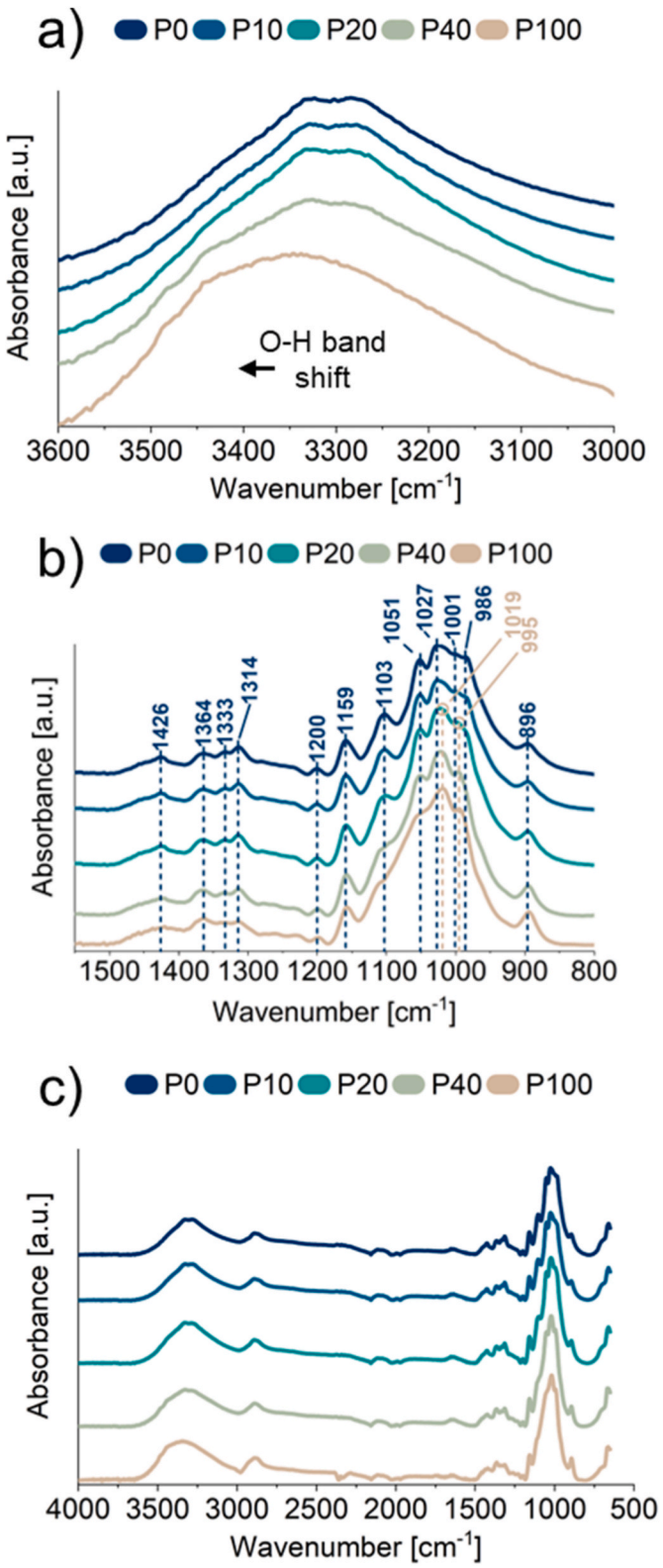

Fig. 6. FT-IR spectra of the precursors, with a detailed view of (a) the OH-stretching region, (b) the fingerprint region and (c) the full spectra.

390 °C (Fig. 8, b) that is absent in the other precursors. In this temperature window, molten KOH migrates inward and reacts with formerly untouched material, producing the additional mass loss observed in P40. These results confirm that P40 retains more unreacted domains up to this point than the other CMS-containing papers, emphasizing its uneven KOH distribution. Activation and significant pore development begin at around 400 °C, accompanied by dehydration processes and the release of non-condensable gases. Dehydration of KOH to K_2O initiates physical activation via the water-gas ($C + H_2O \rightarrow CO + H_2$) and water-gas-shift ($CO + H_2O \rightarrow CO_2 + H_2$) reactions, contributing to mass loss via the etching of the carbon by the emerging gases (H_2O, H_2, CO, CO_2). Simultaneously, redox reactions ($6\,KOH + 2\,C \rightarrow 2\,K + 3H_2 + 2\,K_2CO_3$) also begin near 400 °C and complete KOH → K_2CO_3 conversion by ~600 °C, resulting in the intercalation of metallic K and spreading apart of carbon layers [52]. Mass loss declines until K_2CO_3 decomposition >700 °C produces CO_2, which gasifies carbon via the reverse Boudouard reaction, widening ultramicropores into larger micropores or mesopores [53,54]. Finally, during isothermal activation at 750 °C (Fig. 8, c), P40 shows anomalously high mass loss, indicating over-etching. Solid K_2CO_3 accumulates in regions where KOH closely contacts the carbon precursor, predominantly around CMS, which were unevenly distributed in P40. Previous research has demonstrated that high local concentrations of the activating agent can lead to pore contraction due to complete collapse of the cellulose structure in these areas during heating [42]. Conversely, in regions lacking K_2CO_3, such as former fiber interiors, pore widening is limited. This interpretation is supported by EDX analysis, which reveals pronounced spatial variations in potassium distribution in P40, including a potassium-rich CMS layer on the surface (Fig. 7, j). Regions with locally elevated potassium concentrations correspond to the zones of accelerated mass loss observed in TGA, confirming that the over-activation originates from an uneven distribution of the activating agent. In contrast, samples P10, P20, and P100 exhibit a uniform distribution of CMS, which prevents the emergence of large high-reactivity zones. As a result, activation proceeds in a slower, homogeneous fashion, allowing pores to widen without structural failure.

3.3. AC properties

For SEM analysis (Fig. 9), the ACs were examined without prior grinding to preserve the original morphology. Images of the AC0-AC40 particle surfaces reveal a continuous, foam-like pore network, occasionally interrupted by large voids. The development of macroporosity in the AC series (AC0 → AC100) is primarily dictated by two precursor properties: packing density and cellulose crystallinity. In the fiber-only paper (P0), large inter-fiber voids maintain a low bulk density and create a coarse template for the resulting AC structure. The semi-crystalline cellulose I fibers restrict potassium KOH penetration to a large extent (Fig. 7), limiting carbon removal and resulting in thick residual pore walls after activation. When 10–20 w.% CMS are added, these inter-fiber voids are only partially filled. As a result, the paper becomes less porous, but micron-scale voids persist. However, the cellulose II within each microsphere is much more accessible to KOH than the surrounding fibers, enabling more extensive carbon removal and thinning the carbon framework. At a CMS content of 40 w.%, the microspheres are densely packed, effectively plugging more inter-fiber channels and significantly increasing the precursor's density while reducing the size of initial cavities. During activation, the carbon within these large CMS domains is etched more extensively, as there are less regions shielded from the activator. This results in even thinner pore walls compared to P0–P20. However, because the initial pore size prior to activation is smaller, the resulting macropores remain also smaller after etching. In contrast, the CMS powder (P100) lacks a fibrous network, resulting in large inter-particle voids. Each sphere presents a highly accessible, low-crystallinity surface, allowing KOH to attack radially from all sides. This leads to the fusion of neighboring cavities and a greater degree of carbon removal, ultimately producing the largest macropores and the thinnest walls among all samples.

TEM imaging reveals that incorporating 40 w.% CMS (AC40) transforms the carbon structure of AC from blank paper (AC0) from a fully turbostratic solid into a more open, ribbon-like network. At the coarsest

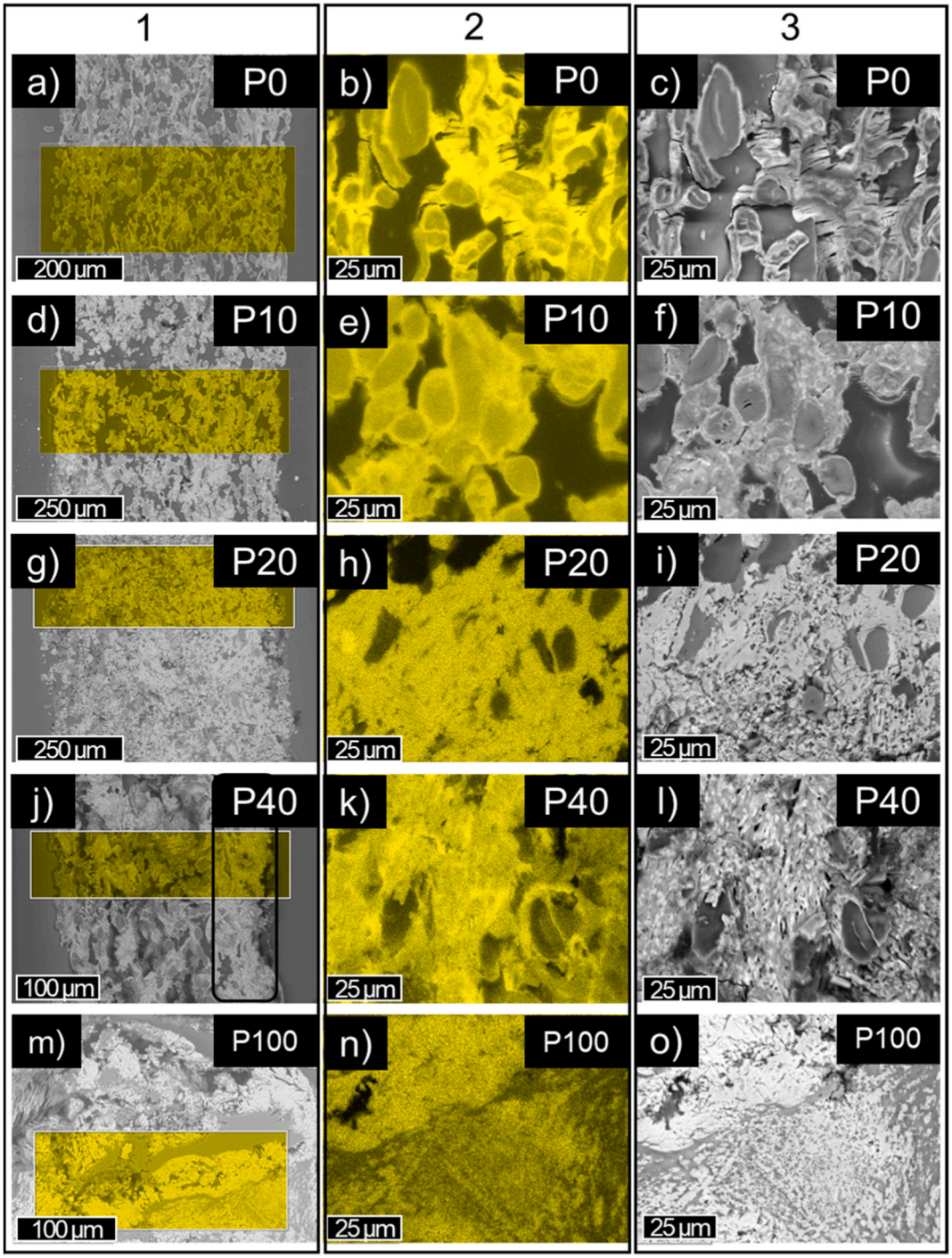

Fig. 7. Overview of backscattered electron (BSE) SEM images with EDX mapping for selected regions (column 1), high-resolution EDX maps highlighting potassium distributions (column 2), and corresponding high-magnification BSE SEM images (column 3) of cross-sections of KOH-impregnated paper and CMS powder.

scale (Fig. 10a and b) and at 150000 × (Fig. 10c and d), the micropores of AC40 appear larger than those of AC0, although both samples retain numerous sub-nanometer pores. At the highest magnification (500 k; Fig. 10e and f), and especially in the zoom images (g, h), AC0 shows pores embedded within a continuous dark matrix, while AC40 presents curved, dark carbon strands that enclose irregular, interconnected cavities, some of which merge over a few nanometers. This morphology indicates that AC40 has lost more amorphous carbon to etching processes, leaving behind thinner, curved carbon ribbons. Such structural evolution reflects a higher activation degree, which can be attributed to the superior contact between CMS and KOH in AC40.

The volume-weighted differential pore size distribution (PSD) obtained from SAXS (Fig. 11, a) reveals a hierarchical micropore structure. This supports the presence of sub-nanometer pores observed in the TEM images (Fig. 10) and confirms that all the ACs studied are predominantly microporous, with most pore diameters falling between 0.1 and 1.0 nm. The mode pore diameter, defined as the diameter at which the differential volume-weighted PSD reaches its maximum, indicates where most of the pore volume is concentrated. It is 0.32 nm for AC0 and 0.35 nm for AC100 (ACs derived from the individual components), while for the ACs derived from composites (AC10-AC40) it is around 0.45 nm. Although increasing CMS content in the precursors of AC10-AC40 does not further

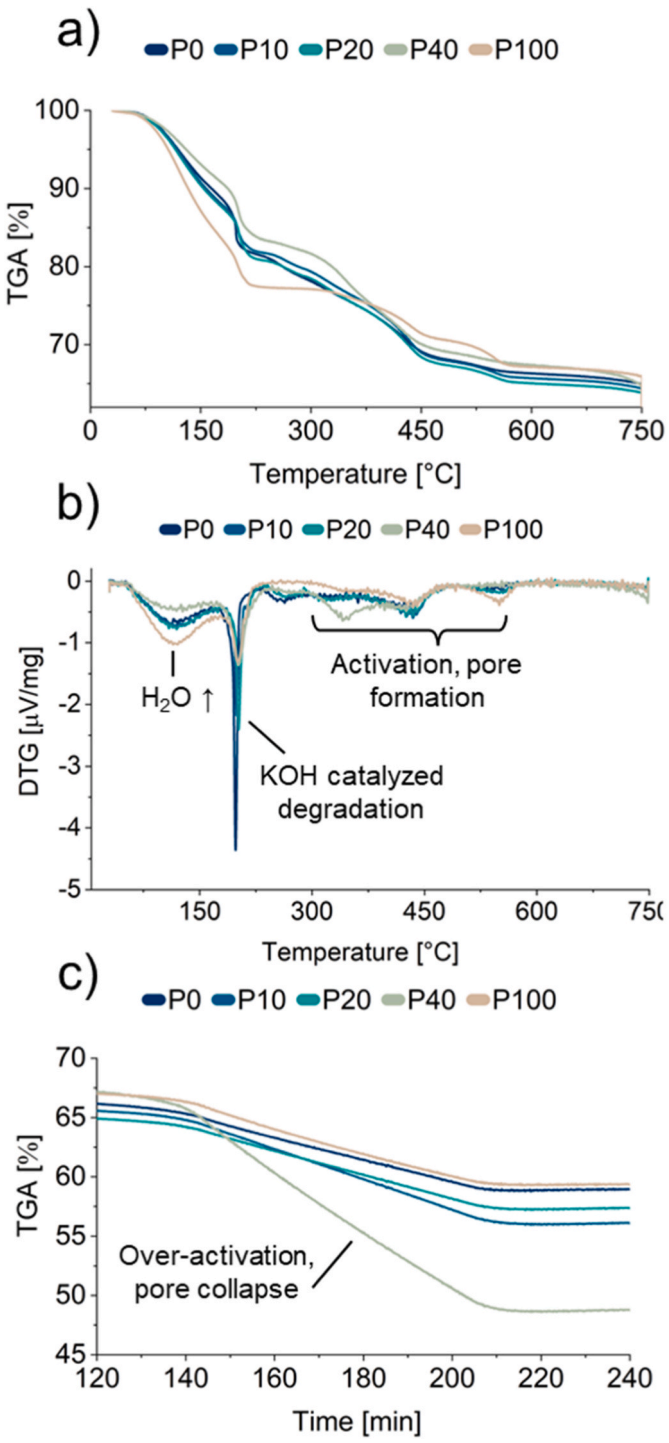

Fig. 8. TGA analysis of KOH-impregnated precursors: a) TGA curves and b) corresponding DTG curves during heating to 750 °C, c) TGA curve recorded during the isothermal 1-h activation step at 750 °C.

shift the mode diameter, it clearly increases the peak height, meaning that a larger fraction of each sample's pore volume is concentrated near the mode. The concurrent rise in SSA suggests that this stronger localization of ultramicroporosity is accompanied by an absolute increase in microporous surface area. As shown by EDX analysis (Fig. 7), this effect can be attributed to the more effective impregnation of CMS by KOH. Unlike fibers, where KOH tends to accumulate on the outer surfaces, the lower crystallinity of CMS enables closer contact between KOH and the carbon. Furthermore, IGC results (Fig. 5, a) indicate that the accessible surface area of samples increases with CMS content (P0–P40). Together, these factors create more etching sites, leading to increased pore formation. However, at approximately 0.8 nm, the PSD curve of AC40 falls below that of AC20 (Fig. 11, a, highlighted area), indicating that AC40 developed fewer larger pores. This observation aligns with our TGA data, as P40 experienced pore contraction during activation at 750 °C.

Beyond an initial slight SSA drop (Fig. 11, c) when adding 10 w.% CMS, the SSA of the paper-derived ACs steadily increases with CMS content from 1887 m^2/g to 2484 m^2/g, and increased greatly for pure CMS-derived AC (3637 m^2/g). This trend displays the rise in pore volume with CMS loading of the precursors.

PSD analysis by N_2 adsorption (Fig. 12, a) has some inherent limitations: the instrument only captured open pores ≥0.89 nm (≥0.97 nm in AC10), so the bulk of ~0.4 nm micropores remain undetected, yielding a distorted picture of the PSD. In our samples, the discrepancies between SAXS- and N_2-derived PSDs and SSAs cannot be explained by N_2 size exclusion alone. TGA and SEM/EDX results, particularly for P40, reveal heterogeneous K distribution and localized over-activation, which caused partial pore collapse. These blocked or ink-bottle pores are still detected by SAXS, which measures all internal interfaces, but remain inaccessible to N_2 molecules. This effect further contributes to the discrepancy between SAXS and BET results. Therefore, the absence of a clear trend in BET-derived SSA (Fig. 12, b) does not represent the actual porosity but instead reflects the limited accessibility of sub-nanometer pores to N_2 and the presence of partially blocked pores. However, a sharp increase in pore volume at ~1 nm confirms high microporosity, in agreement with SAXS (Fig. 11, a). The micropores around 1 nm dominate the SSA calculated via the BET method from N_2 isotherms, leading to a pore-volume/SSA ranking AC20 > AC0 > AC100 > AC40 > AC10, which differs from SAXS-derived PSD and SSA. Additionally, N_2 experiments reveal a drop in pore volume between 1.3 nm and 2.2 nm, followed by a rise that levels off around 4.5 nm, contrasting the profile from SAXS. These discrepancies likely stem from measurement- or sample-specific accessibility limitations for N_2 molecules. However, for mesopores ≥2.4 nm, both SAXS and N_2 data agree on the trend AC100 > AC20 > AC40 ~ AC10 > AC0, reaffirming that AC40 has reduced mesoporous volume. This agreement indicates that the differences between the two methods are confined to the micro- and ultramicropore regime, where pore blocking and diffusion constraints are most relevant. The PSD peak at 5 nm likely does not represent actual pores of that size but instead arises as an artifact from cavitation induced evaporation: larger pores with narrow necks appear as smaller pores when using desorption-based PSD analysis. Consequently, these features are considered as artifacts and are not discussed further here [55].

Table 2 shows that the total pore volume correlates with the BET SSA, as both parameters reflect the extent of accessible porosity. Although the BET SSA of AC100 is higher than that of AC10 and AC40, its micropore surface area and volume are the lowest among all samples, suggesting it is the least microporous. This is reflected in its SSA micro/SSA ratio of only 62 %, compared to 80–87 % for the other samples. However, this conclusion is misleading because N_2 adsorption only probes pores ≥0.89 nm (≥0.97 nm in AC10), whereas SAXS detects all pores. SAXS results therefore provide a more complete picture and reveal that AC100 is actually the most microporous sample, with the majority of its pore volume centered around 0.35 nm (Fig. 11, a), far below the detection limit of N_2 adsorption. The relatively high total BET SSA of AC100, despite its low N_2-derived microporosity, indicates that it contains a larger fraction of N_2-accessible mesopores, consistent with the pronounced shoulder in the N_2 PSD (Fig. 12, a, Table 3).

3.4. Comparison of SAXS derived pore structure and yield of ACs from precursors with varying CMS contents

A comprehensive comparison of the SAXS-derived results reveals that the pore architecture evolves systematically with increasing CMS content in the precursor. The SSA increases from 1887 m^2/g (AC0) to

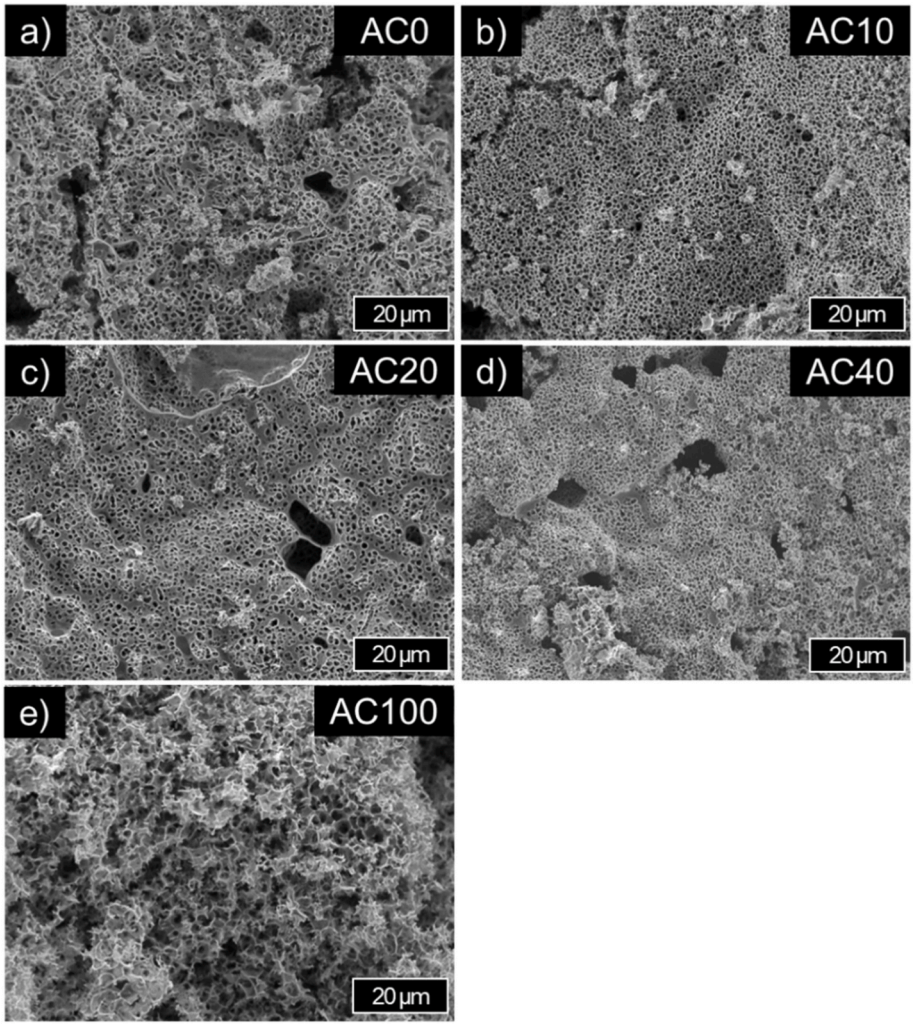

Fig. 9. Microstructures of (a) AC0, (b) AC10, (c) AC20, (d) AC40 and (e) AC100 observed by SEM at 3000 × magnification.

3637 m^2/g (AC100), while the carbon yield (mass of washed AC relative to the dry precursor) decreases from 9.31 w.% to 1.72 w.%. This inverse relationship is characteristic of stronger KOH etching, where more extensive burn-off produces higher surface area but less residual carbon. The concurrent rise in PSD peak height from 42.65 %/nm (AC0) to 77.30 %/nm (AC100), together with the increasing SSA from AC0 to AC40, indicates an absolute growth in microporous surface area with higher CMS content.

The volume fraction of pores ≥1 nm remains below 2.6 % for AC0–AC20, drops to 0.6 % for AC40, and reaches a maximum of 5.4 % in AC100. The reduction of larger pores in AC40 reflects the uneven activation, caused by non-uniform KOH distribution due to the heterogeneous dispersion of CMS (Fig. 7, j). This results in pore collapse in over-activated regions and limited pore widening in potassium-deficient zones. In contrast, AC100 exhibits both a pronounced ultramicropore peak and an increased ≥1 nm fraction, indicative of a more hierarchical micro-/mesoporous network.

The combination of a large CMS fraction and its homogeneous distribution across the precursor cross-section (Fig. 7, g) in AC20 enables consistent activation that yields a high ultramicropore volume and, unlike AC40, also generates pores larger than 1 nm. The most diverse and well-developed pore structure is observed in AC100, where accessibility limitations are minimized because the less crystalline CMS particles are uniformly exposed to KOH. However, this comes at the cost of a very low carbon yield. Considering both surface area and yield, AC20 offers a favorable compromise, combining high SSA, moderate numbers of larger pores, and a fourfold higher yield compared to AC100. If maximizing ultramicropore volume is the primary objective, AC40 is best.

4. Conclusion

This study demonstrates that systematically tuning precursor microstructure strongly influences the properties of AC produced via one-step KOH activation. Increasing the CMS content effectively reduces precursor crystallinity, as confirmed by WAXS and FTIR. The resulting decrease in crystallinity and increase in precursor SSA improve KOH accessibility and impregnation, thereby enhancing the interaction between the activator and cellulose. This was further supported by SEM-EDX, which showed that CMS-rich regions allowed deeper potassium penetration than the more crystalline fibers. Following thermal activation, these structural variations in the precursor directly determined the morphology and pore architecture of the resulting carbons. With increasing CMS content, the carbon structure transitioned from turbostratic domains to more open, ribbon-like morphologies with thinner pore walls. Higher CMS loadings generally correlated with increased SAXS-derived SSAs (1887–3637 m^2/g) and enhanced sub-nanometer porosity, confirming that precursor-structure engineering is an effective approach for tailoring AC properties.

In addition to modifying the microstructure of the precursor to improve cellulose-KOH contact, increasing the KOH-to-precursor mass ratio can also enhance microporosity up to an optimal level [16,22].

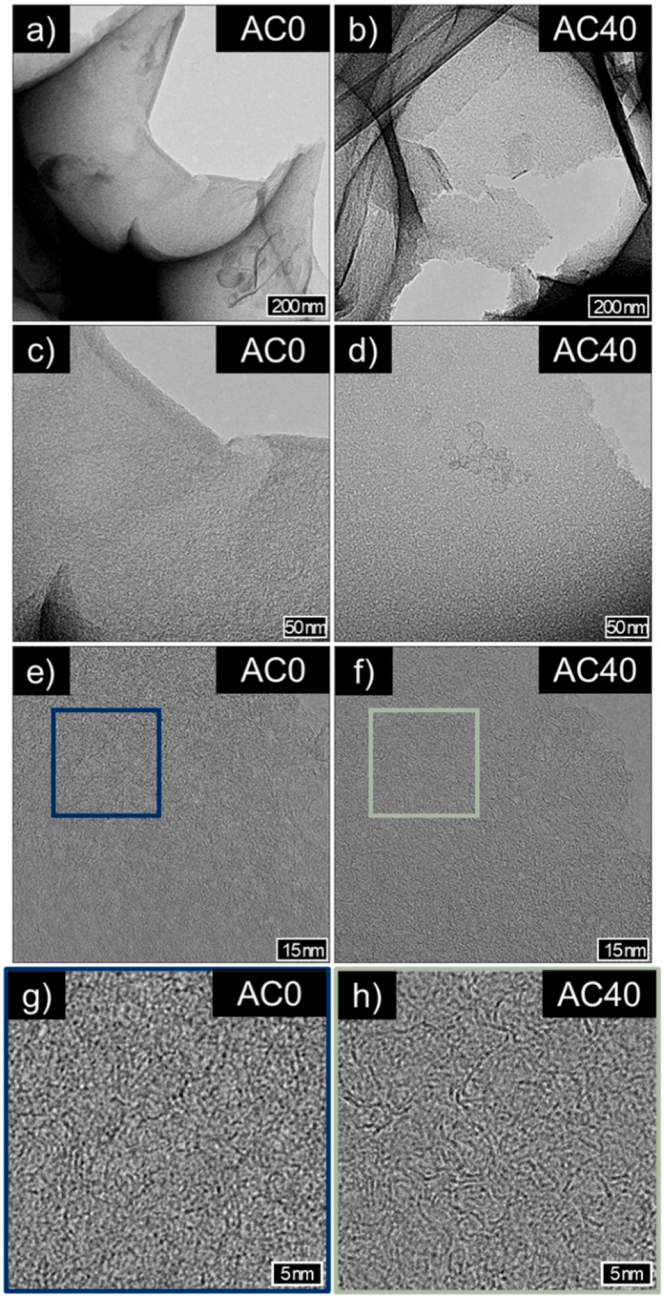

Fig. 10. Nanostructures of AC0 and AC40 observed by TEM: (a, b) at 50,000 × magnification, (c, d) at 150,000 × , (e, f) at 500,000 × , and (g, h) zoom-ins of the 500,000 × images.

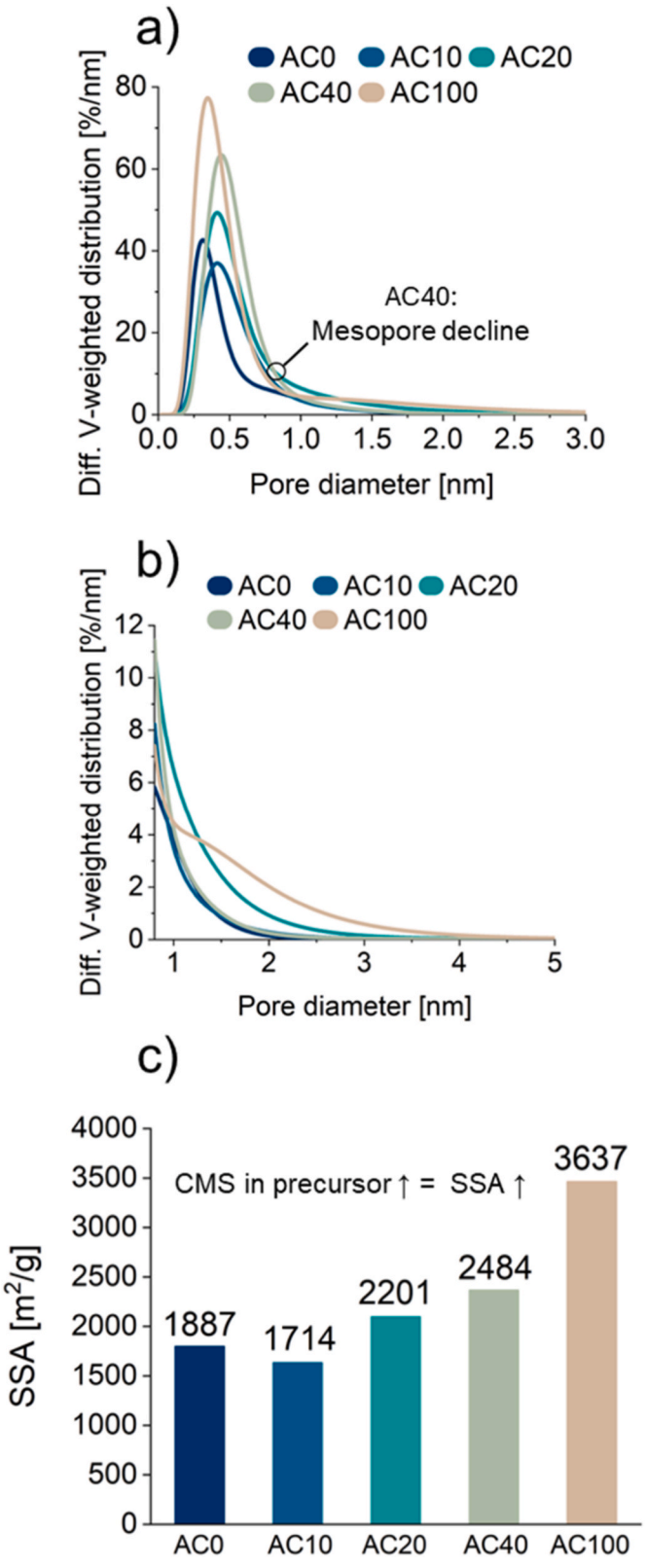

Fig. 11. Differential volume-weighted PSD of ACs determined by SAXS: a) PSD curves in the (ultra-)micropore size range, b) zoom-in on the mesopore region, c) SSA calculated from SAXS data.

However, this approach is neither sustainable nor economical, as it requires large amounts of activating agent, and ratios above approximately 1.5:1 (KOH:precursor) lead to excessive etching, causing pore collapse [56]. Adjusting other process parameters, such as activation time or temperature, primarily affects the activation mechanism through enhanced carbon gasification, which promotes pore widening [56–58]. While moderate increases in these parameters may improve activation outcomes for precursors with higher crystallinity, excessive intensification leads to structural degradation.

However, the high accessibility of CMS to KOH also introduced challenges. In samples with uneven CMS distribution, such as P40, local potassium concentration gradients developed, resulting in non-uniform activation. This effect manifested in TGA as anomalously high mass loss and structural degradation, which in turn caused a reduction in

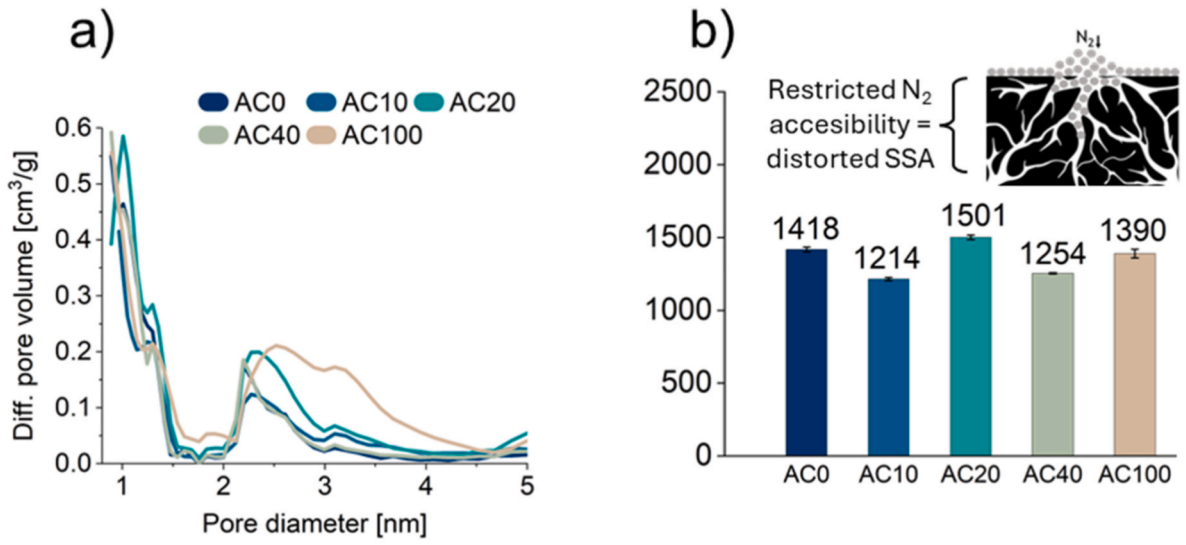

Fig. 12. Differential pore volume distributions of ACs determined by N_2 adsorption: a) PSD curves, b) SSA calculated from N_2 adsorption data.

Table 2
Summary of N_2 adsorption results for AC0-AC100. Listed are the SSA, total pore volume, micropore SSA and volume (t-plot, pores <2 nm), and the contribution of micropores to the total surface area.

AC	SSA [m^2/g]	Pore volume [cm^3/g]	SSA micro [m^2/g]	Pore volume micro [cm^3/g]	SSA micro/ SSA [%]
AC0	1418	0.8	1239	0.6	87
AC10	1214	0.7	994	0.5	82
AC20	1501	0.9	1202	0.6	80
AC40	1254	0.7	1025	0.5	82
AC100	1390	0.8	864	0.4	62

Table 3
Comparison of SAXS derived properties (SSA, cumulative pore volume fraction) and carbon yields of ACs.

AC	SSA [m^2/g]	C-yield [w.%]	Peak of diff. volume-weighted distribution [%/nm]	Volume fraction of pores ≥1 nm [%]
AC0	1887	9.3	42.7	0.7
AC10	1714	7.8	37.0	1.3
AC20	2201	6.5	49.3	2.6
AC40	2484	5.9	63.4	0.6
AC100	3637	1.7	77.3	5.4

mesoporous volume, as evidenced by SAXS and N_2 adsorption analyses. Such heterogeneous distributions of more and less accessible domains are typical in lignocellulosic biomass. For example, in wood, density differences between earlywood and latewood [59,60] and uneven lignin distribution across cell-wall layers [61]. lead to similar spatial variations in accessibility and thus reactivity. While our all-cellulose composite system does not reproduce the full complexity of biomass, sample P40 illustrates within our model system the consequences of heterogeneous precursor microstructure on KOH activation and the resulting carbon structure. These findings suggest that part of the reproducibility challenges commonly encountered in biomass activation may arise from structural heterogeneity in the precursor. Accounting for crystallinity and density variations, and homogenizing them where possible, could therefore help achieve more consistent activation outcomes.

Our work expands the limited literature on biomass-AC structure relationships by establishing a clear mechanistic link between precursor structure, KOH accessibility, and resulting pore architecture. Beyond these fundamental insights, it identifies precursor-structure engineering as a sustainable route to microporous AC suitable for supercapacitor and CO_2 capture applications. Micropores serve as the primary charge-storage sites, providing a large internal surface area for ion accumulation [9,12,14]. The abundant sub-nanometer pores in the produced ACs facilitate ion desolvation and dense packing, thereby enhancing capacitance and ion transport [10]. Among the composite-derived carbons (AC10, AC20, AC40), AC20 exhibits the most favorable pore structure for supercapacitor applications, combining abundant ultramicropores with a minor fraction of mesopores that aid ion transport. For CO_2 capture, the ultramicropore volume is critical [1,4]. Therefore, AC40, with its largest sub-nanometer pore volume, is the most suitable.

CRediT authorship contribution statement

Alexa Scheer: Writing – original draft, Methodology, Formal analysis, Conceptualization. **Glen J. Smales:** Writing – review & editing, Writing – original draft, Methodology, Formal analysis. **Hoang Bao Tran Nguyen:** Writing – review & editing, Methodology, Formal analysis. **Johannes Rattenberger:** Writing – review & editing, Methodology, Formal analysis. **Claudia Mayrhofer:** Methodology. **Johanna Fischer:** Writing – review & editing, Methodology, Conceptualization. **Steffen Fischer:** Writing – review & editing, Resources, Project administration, Funding acquisition, Conceptualization. **Daria Mikhailova:** Writing – review & editing, Resources, Project administration, Funding acquisition, Conceptualization. **Stefan Spirk:** Writing – review & editing, Supervision, Resources, Project administration, Funding acquisition, Conceptualization.

Declaration of competing interest

The authors declare the following financial interests/personal relationships which may be considered as potential competing interests: Stefan Spirk reports financial support was provided by Austrian Science Fund. If there are other authors, they declare that they have no known competing financial interests or personal relationships that could have appeared to influence the work reported in this paper.

Acknowledgements

This research was funded by the Austrian Science Fund (FWF) [I-6403, Grant doi: 10.55776/I6403]. For the purpose of open access, the author has applied a CC BY public copyright licence to any Author Accepted Manuscript version arising from this submission. The authors

would like to acknowledge use of the Somapp Lab, a core facility supported by the Austrian Federal Ministry of Education, Science and Research, the Graz University of Technology and Anton Paar GmbH. The authors thank Maximilian Fuchs for performing the image analysis of the SEM micrographs.

Appendix A. Supplementary data

Supplementary data to this article can be found online at https://doi.org/10.1016/j.carbon.2025.121036.

References

[1] X. Ma, R. Chen, K.C. Zhou, Q.-d. Wu, H.-l. Li, Z. Zeng, L. Li, Activated porous carbon with an ultrahigh surface area derived from waste biomass for acetone adsorption, CO2 capture, and light hydrocarbon separation, ACS Sustain. Chem. Eng. 8 (2020) 11721–11728, https://doi.org/10.1021/acssuschemeng.0c03725.

[2] J. Park, N.F. Attia, M. Jung, K. Lee, H. Oh, Biobased derived nanoporous carbon for hydrogen isotope separation, Microporous Mesoporous Mater. 304 (2020) 109291, https://doi.org/10.1016/j.micromeso.2019.01.029.

[3] K. Adlak, R. Chandra, V.K. Vijay, K.K. Pant, Physicochemical activation and palletisation of Azadirachta indica wood carbons for increased biomethane adsorbed energy storage, J. Anal. Appl. Pyrolysis 155 (2021) 105102, https://doi.org/10.1016/j.jaap.2021.105102.

[4] K. Park, B. Ko, J. Ahn, T. Park, S.-D. Yoon, W.-G. Shim, S.-H. Song, An ultramicroporous graphene-based 3D structure derived from cellulose-based biomass for high-performance CO2 capture, ACS Appl. Mater. Interfaces 9 (39) (2024), https://doi.org/10.1021/acsami.4c05600.

[5] S. Stock, N. Kostoglou, J. Selinger, S. Spirk, C. Tampaxis, G. Charalambopoulou, T. Steriotis, C. Rebholz, C. Mitterer, O. Paris, Coffee waste-derived nanoporous carbons for hydrogen storage, ACS Appl. Energy Mater. 5 (9) (2022) 10915–10926, https://doi.org/10.1021/acsaem.2c01573.

[6] A.A. Altalhi, E.A. Mohammed, S.S.M. Morsy, N.A. Negm, A.A. Farag, Catalyzed production of different grade biofuels using metal ions modified activated carbon of cellulosic wastes, Fuel 295 (2021) 120646, https://doi.org/10.1016/j.fuel.2021.120646.

[7] D. Higai, C. Lee, J. Lang, E.W. Qian, Saccharification of cellulose using biomass-derived activated carbon-based solid acid catalysts, Fuel Process. Technol. 215 (2021) 106738, https://doi.org/10.1016/j.fuproc.2021.106738.

[8] Y. Li, D. Zhang, Y. Zhang, J. He, Y. Wang, K. Wang, Y. Xu, H. Li, Y. Wang, Biomass-derived microporous carbon with large micropore size for high-performance supercapacitors, J. Power Sources 448 (2020) 227396, https://doi.org/10.1016/j.jpowsour.2019.227396.

[9] Y. Wang, Y. Chen, H. Zhao, L. Li, D.-W. Ju, C. Wang, B. An, Biomass-derived porous carbon with a good balance between high specific surface area and mesopore volume for supercapacitors, Nanomaterials 12 (2022), https://doi.org/10.3390/nano12213804.

[10] L.J. Andrew, E.R. Gillman, C.M. Walters, E. Lizundia, M.J. MacLachlan, Multi-responsive supercapacitors from chiral nematic cellulose nanocrystal-based activated carbon aerogels, Small (2023) e2301947, https://doi.org/10.1002/smll.202301947.

[11] N. Kostoglou, C. Koczwara, S. Stock, C. Tampaxis, G. Charalambopoulou, T. Steriotis, O. Paris, C. Rebholz, C. Mitterer, Nanoporous polymer-derived activated carbon for hydrogen adsorption and electrochemical energy storage, Chem. Eng. J. 427 (2022) 131730, https://doi.org/10.1016/j.cej.2021.131730.

[12] C. Ma, Q. Fan, M. Dirican, N. Subjalearndee, H. Cheng, J. Li, Y. Song, J. Shi, X. Zhang, Rational design of meso-/micro-pores for enhancing ion transportation in highly-porous carbon nanofibers used as electrode for supercapacitors, Appl. Surf. Sci. 545 (2021) 148933, https://doi.org/10.1016/j.apsusc.2021.148933.

[13] Y. Zhou, J. Li, S. Hu, G. Qian, J. Shi, S. Zhao, Y. Wang, C.-G. Wang, J. Lian, Sawdust-derived activated carbon with hierarchical pores for high-performance symmetric supercapacitors, Nanomaterials 12 (2022), https://doi.org/10.3390/nano12050810.

[14] J. Selinger, K. Meinander, B.P. Wilson, Q. Abbas, M. Hummel, S. Spirk, Sweet side streams: sugar beet pulp as source for high-performance supercapacitor electrodes, ACS Omega 9 (4) (2024) 4733–4743, https://doi.org/10.1021/acsomega.3c07976.

[15] L.S. Blankenship, R. Mokaya, Modulating the porosity of carbons for improved adsorption of hydrogen, carbon dioxide, and methane: a review, Mater. Adv. 3 (4) (2022) 1905–1930, https://doi.org/10.1039/D1MA00911G.

[16] O. Oginni, K. Singh, G. Oporto, B. Dawson-Andoh, L. McDonald, E. Sabolsky, Influence of one-step and two-step KOH activation on activated carbon characteristics, Bioresour. Technol. Rep. 7 (2019) 100266, https://doi.org/10.1016/j.biteb.2019.100266.

[17] Y. Li, B. Xing, Y. Ding, X. Han, S. Wang, A critical review of the production and advanced utilization of biochar via selective pyrolysis of lignocellulosic biomass, Bioresour. Technol. 312 (2020) 123614, https://doi.org/10.1016/j.biortech.2020.123614.

[18] Y. Fu, Y. Shen, Z. Zhang, X. Ge, M. Chen, Activated bio-chars derived from rice husk via one- and two-step KOH-catalyzed pyrolysis for phenol adsorption, Sci. Total Environ. 646 (2019) 1567–1577, https://doi.org/10.1016/j.scitotenv.2018.07.423.

[19] Y. Li, Z.-H. Sun, L. Zhang, Y. Zou, N. Yao, W. Lei, T. Jiang, Y. Chen, G.Z. Chen, High yield and packing density activated carbon by one-step molecular level activation of hydrophilic pomelo peel for supercapacitors, J. Electrochem. Soc. 168 (2021) 060521, https://doi.org/10.1149/1945-7111/ac0762.

[20] L. Zhu, Q. Wang, H. Wang, F. Zhao, D. Li, One-step chemical activation facilitates synthesis of activated carbons from Acer truncatum seed shells for premium capacitor electrodes, Ind. Crop. Prod. 187 (2022) 115458, https://doi.org/10.1016/j.indcrop.2022.115458.

[21] L. Zhang, H. Gu, H. Sun, F. Cao, Y. Chen, G.Z. Chen, Molecular level one-step activation of agar to activated carbon for high performance supercapacitors, Carbon 132 (2018) 573–579, https://doi.org/10.1016/j.carbon.2018.02.100.

[22] W. Chen, M. Gong, K. Li, M. Xia, Z. Chen, H. Xiao, Y. Fang, Y. Chen, H. Yang, H. Chen, Insight into KOH activation mechanism during biomass pyrolysis: chemical reactions between O-containing groups and KOH, Appl. Energy 278 (2020) 115730, https://doi.org/10.1016/j.apenergy.2020.115730.

[23] J.A. Maciá-Agulló, B.C. Moore, D. Cazorla-Amorós, A. Linares-Solano, Influence of carbon fibres crystallinities on their chemical activation by KOH and NaOH, Microporous Mesoporous Mater. 101 (3) (2007) 397–405, https://doi.org/10.1016/j.micromeso.2006.12.002.

[24] S. Zuo, J. Liu, J. Yang, X. Cai, Effects of the crystallinity of lignocellulosic material on the porosity of phosphoric acid-activated carbon, Carbon 47 (15) (2009) 3578–3580, https://doi.org/10.1016/j.carbon.2009.08.026.

[25] J.B. Schaubeder, C. Guizani, J. Selinger, A. Mautner, M. Hummel, S. Spirk, Design of experiments as a tool to guide the preparation of tailor-made activated carbons, Sci. Rep. 13 (1) (2023) 3977, https://doi.org/10.1038/s41598-023-30642-8.

[26] M. Iwanow, T. Gärtner, V. Sieber, B. König, Activated carbon as catalyst support: precursors, preparation, modification and characterization, Beilstein J. Org. Chem. 16 (2020) 1188–1202, https://doi.org/10.3762/bjoc.16.104.

[27] G. Li, A. Iakunkov, N. Boulanger, O.A. Lazar, M. Enachescu, A. Grimm, A. V. Talyzin, Activated carbons with extremely high surface area produced from cones, bark and wood using the same procedure, RSC Adv. 13 (21) (2023) 14543–14553, https://doi.org/10.1039/D3RA00820G.

[28] E. Yagmur, Y. Gokce, S. Tekin, N.I. Semerci, Z. Aktas, Characteristics and comparison of activated carbons prepared from oleaster (Elaeagnus angustifolia L.) fruit using KOH and ZnCl2, Fuel 267 (2020) 117232, https://doi.org/10.1016/j.fuel.2020.117232.

[29] R. Xiong, Y. Zhang, W. Zhou, K. Xia, Q. Sun, G. Chen, B. Han, Q. Gao, C. Zhou, Chemical activation of carbon materials for supercapacitors: elucidating the effect of spatial characteristics of the precursors, Colloids Surf. A Physicochem. Eng. Asp. 597 (2020) 124762, https://doi.org/10.1016/j.colsurfa.2020.124762.

[30] A. Scheer, J. Fischer, A. Bakhshi, W. Bauer, S. Fischer, S. Spirk, Fusion of cellulose microspheres with pulp fibers: creating an unconventional type of paper, Carbohydr. Polym. 338 (2024) 122207, https://doi.org/10.1016/j.carbpol.2024.122207.

[31] K. Thümmler, S. Fischer, A. Feldner, V. Weber, M. Ettenauer, F. Loth, D. Falkenhagen, Preparation and characterization of cellulose microspheres, Cellulose 18 (2011) 135–142, https://doi.org/10.1007/s10570-010-9465-z.

[32] J. Filik, A.W. Ashton, P.C.Y. Chang, P.A. Chater, S.J. Day, M. Drakopoulos, M. W. Gerring, M.L. Hart, O.V. Magdysyuk, S. Michalik, A. Smith, C.C. Tang, N. J. Terrill, M.T. Wharmby, H. Wilhelm, Processing two-dimensional X-ray diffraction and small-angle scattering data in DAWN 2, J. Appl. Crystallogr. 50 (3) (2017) 959–966, https://doi.org/10.1107/S1600576717004708.

[33] N.C. Murillo, P. Szymoniak, G.J. Smales, H. Sturm, A. Schönhals, Electrospun nanocomposite fibers of Polycarbonate- and taurine-modified boehmite nanoparticles: what can be learned from structural and thermal investigations? ACS Appl. Polym. Mater. 3 (12) (2021) 6572–6585, https://doi.org/10.1021/acsapm.1c01265.

[34] P. Szymoniak, B.R. Pauw, X. Qu, A. Schönhals, Competition of nanoparticle-induced mobilization and immobilization effects on segmental dynamics of an epoxy-based nanocomposite, Soft Matter 16 (23) (2020) 5406–5421, https://doi.org/10.1039/D0SM00744G.

[35] I. Bressler, J. Kohlbrecher, A.F. Thunemann, SASfit: a tool for small-angle scattering data analysis using a library of analytical expressions, J. Appl. Crystallogr. 48 (5) (2015) 1587–1598, https://doi.org/10.1107/S1600576715016544.

[36] S. Brunauer, P.H. Emmett, E. Teller, Adsorption of gases in multimolecular layers, J. Am. Chem. Soc. 60 (2) (1938) 309–319, https://doi.org/10.1021/ja01269a023.

[37] R.W. Magee, Evaluation of the external surface area of carbon black by nitrogen adsorption, Rubber Chem. Technol. 68 (4) (1995) 590–600, https://doi.org/10.5254/1.3538760.

[38] P.I. Ravikovitch, A.V. Neimark, Density functional theory model of adsorption on amorphous and microporous silica materials, Langmuir 22 (26) (2006) 11171–11179, https://doi.org/10.1021/la0616146.

[39] M. Thommes, Physical adsorption characterization of nanoporous materials, Chem. Ing. Tech. 82 (7) (2010) 1059–1073, https://doi.org/10.1002/cite.201000064.

[40] D.V. Zlenko, D.N. Vtyurina, S.V. Usachev, A.A. Skoblin, M.G. Mikhaleva, G. G. Politenkova, S.N. Nikolsky, S.V. Stovbun, On the orientation of the chains in the mercerized cellulose, Sci. Rep. 11 (1) (2021) 8765, https://doi.org/10.1038/s41598-021-88040-x.

[41] Z. Ling, S. Chen, X. Zhang, K. Takabe, F. Xu, Unraveling variations of crystalline cellulose induced by ionic liquid and their effects on enzymatic hydrolysis, Sci. Rep. 7 (1) (2017) 10230, https://doi.org/10.1038/s41598-017-09885-9.

[42] A. Merlini, V.C. De Souza, R.M. Gomes, A. Coirolo, S. Merlini, R.A.F. Machado, Effects of reaction conditions on the shape and crystalline structure of cellulose nanocrystals, Cellul. Chem. Technol. 52 (5–6) (2018) 325–335.

[43] A. Turki, A. El Oudiani, S. Msahli, F. Sakli, Investigation of OH bond energy for chemically treated alfa fibers, Carbohydr. Polym. 186 (2018) 226–235, https://doi.org/10.1016/j.carbpol.2018.01.030.
[44] D.V.C. Schmidt, T.L.G. Costa, D.F. Cipriano, C.S. Meireles, C.J. Dalmaschio, J.C. C. Freitas, Biomass-derived cellulose acetate membranes modified with TiO2/Graphene oxide for oil-in-water emulsion treatment, ACS Omega 9 (39) (2024) 40882–40896, https://doi.org/10.1021/acsomega.4c05980.
[45] M. Fan, D. Dai, B. Huang, Fourier transform infrared spectroscopy for natural fibres, Fourier transform-materials analysis 3 (2012) 45–68.
[46] M.M. Rana, H. De la Hoz Siegler, Influence of ionic liquid (IL) treatment conditions in the regeneration of cellulose with different crystallinity, J. Mater. Res. 38 (2) (2023) 328–336, https://doi.org/10.1557/s43578-022-00797-7.
[47] J. Pang, M. Wu, Q. Zhang, X. Tan, F. Xu, X. Zhang, R. Sun, Comparison of physical properties of regenerated cellulose films fabricated with different cellulose feedstocks in ionic liquid, Carbohydr. Polym. 121 (2015) 71–78, https://doi.org/10.1016/j.carbpol.2014.11.067.
[48] J. Han, C. Zhou, A.D. French, G. Han, Q. Wu, Characterization of cellulose II nanoparticles regenerated from 1-butyl-3-methylimidazolium chloride, Carbohydr. Polym. 94 (2) (2013) 773–781, https://doi.org/10.1016/j.carbpol.2013.02.003.
[49] D. Zhao, H. Feng, Y. Wang, F. Wang, H. Wang, H. Liu, H. Liu, Influence mechanism of K on cellulose pyrolysis by stepwise isothermal method in-situ DRIFTS method, Fuel 360 (2024) 130601, https://doi.org/10.1016/j.fuel.2023.130601.
[50] Y. Le Brech, T. Ghislain, S. Leclerc, M. Bouroukba, L. Delmotte, N. Brosse, C. Snape, P. Chaimbault, A. Dufour, Effect of potassium on the mechanisms of biomass pyrolysis studied using complementary analytical techniques, ChemSusChem 9 (8) (2016) 863–872, https://doi.org/10.1002/cssc.201501560.
[51] K. Wang, S. Xu, Preparation of high specific surface area activated carbon from petroleum coke by KOH activation in a rotary kiln, Processes 12 (2) (2024) 241, https://doi.org/10.3390/pr12020241.
[52] S.G. Wabo, O. Klepel, Nitrogen release and pore formation through KOH activation of nitrogen-doped carbon materials: an evaluation of the literature, Carbon Lett. 31 (4) (2021) 581–592, https://doi.org/10.1007/s42823-021-00252-3.
[53] D. Zhao, K. Chen, F. Yang, G. Feng, Y. Sun, Y. Dai, Thermal degradation kinetics and heat properties of cellulosic cigarette paper: influence of potassium carboxylate as combustion improver, Cellulose 20 (6) (2013) 3205–3217, https://doi.org/10.1007/s10570-013-0024-2.
[54] Z. Li, X. Gao, L. Wu, K. Wang, N. Kobayashi, Preparation of activated carbons from poplar wood by chemical activation with KOH, J. Porous Mater. 24 (1) (2017) 193–202, https://doi.org/10.1007/s10934-016-0252-6.
[55] M. Thommes, K.A. Cychosz, A.V. Neimark, Advanced Physical Adsorption Characterization of Nanoporous Carbons, Novel Carbon Adsorbents2012, pp. 107-145.
[56] G. Harimisa, N. Jusoh, L. Tan, K. Shameli, N. Ghafar, A. Masudi, Synthesis of potassium hydroxide-treated activated carbon via one-step activation method. Journal of Physics: Conference Series, IOP Publishing, 2022 012009, https://doi.org/10.1088/1742-6596/2259/1/012009.
[57] J. Cheng, S.-C. Hu, G.-T. Sun, K. Kang, M.-Q. Zhu, Z.-C. Geng, Comparison of activated carbons prepared by one-step and two-step chemical activation process based on cotton stalk for supercapacitors application, Energy 215 (2021) 119144, https://doi.org/10.1016/j.energy.2020.119144.
[58] Y. Gao, Q. Yue, B. Gao, A. Li, Insight into activated carbon from different kinds of chemical activating agents: a review, Sci. Total Environ. 746 (2020) 141094, https://doi.org/10.1016/j.scitotenv.2020.141094.
[59] Ü. Büyüksarı, N. As, T. Dündar, Mechanical properties of earlywood and latewood sections of Scots pine wood, Bioresources 12 (2) (2017) 4004–4012, https://doi.org/10.15376/biores.12.2.4004-4012.
[60] J. Björklund, K. Seftigen, F. Schweingruber, P. Fonti, G. von Arx, M. V. Bryukhanova, H.E. Cuny, M. Carrer, D. Castagneri, D.C. Frank, Cell size and wall dimensions drive distinct variability of earlywood and latewood density in Northern Hemisphere conifers, New Phytol. 216 (3) (2017) 728–740, https://doi.org/10.1111/nph.14639.
[61] L. Zhang, A. Larsson, A. Moldin, U. Edlund, Comparison of lignin distribution, structure, and morphology in wheat straw and wood, Ind. Crop. Prod. 187 (2022) 115432, https://doi.org/10.1016/j.indcrop.2022.115432.